Collective dynamics of flowing colloids during pore clogging†

Gbedo Constant Agbangla,[abe] Patrice Bacchin*[abe] and Eric Climent[cde]

Based on direct numerical simulations of the coupled motion of particles and fluid, this study analyzes the collective hydrodynamic and colloidal effects of flowing microparticles during the formation of different 3D clogging patterns at a pore entrance. Simulations of flowing suspensions through a pore with various simulation conditions show that particle concentration and surface interactions play a major role in the occurrence of the bridging phenomenon (simultaneous adhesion of many particles). In the absence of DLVO repulsive forces, plugging is characterized by the temporal reduction of the bulk permeability when increasing the volume fraction of the flowing suspension up to 20%. Under these conditions, different structures of particle aggregates (from cluster to cake plug) are formed at the pore entrance yielding different evolution rates of hydrodynamic resistance to the flow. Taking into account DLVO repulsive forces in simulations for a particle concentration equal to 10%, we observe the transition from dendritic structures (for low repulsion) to dense aggregates (for high repulsion). At high DLVO repulsive forces, the scenario of pore clogging is controlled by the collective behavior of many interacting particles. It leads to the formation of a jamming phase (Wigner glass phase) with transient clusters of interacting particles at the pore entrance. The network of jammed particles collapses when the force chains among the particles are overcome by the flow stress. The build-up and the collapse of the jammed phase at the pore entrance induce temporal permeability fluctuations. According to the relative magnitude of particle–particle and particle–wall interactions, when the jammed phase is disorganized by the flow, the residual force in the network can accelerate particles and lead to particle adhesion at the wall inducing a pore blockage and a rapid reduction of the bulk permeability.

DOI: 10.1039/c4sm00869c

1 Introduction

The physics of concentrated flowing suspension is still a scientific challenge meeting applications in many engineering processes. For example, separation techniques such as microfiltration or ultrafiltration, require a comprehensive description of the behavior of microparticles passing through a pore to prevent the occurrence of fouling which is still the major limiting phenomenon. Several studies have been performed to find optimal operating conditions which prevent or limit fouling. Different experimental techniques and numerical approaches have been developed to gain insight into the kinetics of blockage in filtration and on the spatial structure of particle aggregates.

[a]Université de Toulouse, INPT, UPS Laboratoire de Génie Chimique, 118 Route de Narbonne, F-31062 Toulouse, France. E-mail: bacchin@chimie.ups-tlse.fr
[b]CNRS, UMR 5503, F-31062 Toulouse, France
[c]Université de Toulouse, INPT, UPS, Institut de Mécanique des Fluides, Allée Camille Soula, F-31400 Toulouse, France
[d]CNRS, UMR 5502, F-31400 Toulouse, France
[e]CNRS, Fédération de Recherche FERMAT, Toulouse, France

† Electronic supplementary information (ESI) available: Videos. See DOI: 10.1039/c4sm00869c

However, this problem is rather complex because of the interplay of various forces and mechanisms. Recently, the direct visualization of micropore fouling has been made possible by new progresses in the micro-device fabrication technology. At the pore scale, Mustin *et al.*[1] have studied experimentally, the effect of the particle size distribution (ranging from 0.47 μm to 1.5 μm) on the dynamics of microchannel blocking during filtration experiments performed under constant pressure drop. According to the particle size distribution, they concluded that deposition of particles in a suspension leading to microsystem clogging occurs through successive particle deposition, particle size exclusion, or through a combination of these effects. Numerically, Kim *et al.*[2] have analyzed the behavior of a particle doublet flowing through a pore in the presence of electrostatic repulsive forces. The Brownian motion of particles is modeled by a stochastic forcing of the particle trajectory (Langevin equation). When repulsive forces are accounted for, a flowing particle can pass through a pore just after the attachment of another particle. This is due to a modification of the hydrodynamics of the fluid flow, the successive repulsion of particles or the Brownian diffusion. Gassara *et al.*[3] have investigated the effect of the particle size on filtration process efficiency in a Hele-Shaw device. They visualized the morphology of particle deposits in the presence of DLVO (attractive and repulsive)

interaction forces. The kinetics of colloids deposit build-up is strongly dependent on surface interactions:[4] below the permeation critical flux, particle–surface repulsive interactions overcome hydrodynamic force preventing adhesion of particles onto a permeable surface. The interplay between the drag force and the colloidal forces leads to a critical transition between a dispersed accumulation and a condensed packed deposit at the pore entrance. Recently, Henry *et al.*[5] used a new Lagrangian stochastic approach to confirm that clogging results from the competition between particle–fluid, particle–surface and particle–particle interactions. Particle deposition is characterized by the formation of either a single monolayer or multilayers of particles depending on hydrodynamical conditions, fluid properties (ionic strength) as well as particle and substrate properties (zeta potentials). The complex interplay between the multi-body surface interactions and hydrodynamic flow in a confined geometry (at pore scale) makes clogging phenomena still unpredictable.[6]

In this context, we investigate the collective dynamics of interacting particles at a pore entrance by using the Force Coupling Method (FCM). A brief description of this method which takes into account hydrodynamic and colloidal interaction forces is given in the next section. Then, we describe the flow configuration and conditions of the simulations performed at the pore scale. Finally, the dynamics of particle aggregation and deposition in the pore is analyzed in terms of the temporal evolution of the bulk permeability, the variation of the additional hydrodynamic resistance and the observation of different 3D structures. Varying the non-hydrodynamic forces from pure adhesion to strong repulsion we show that the morphology of the deposit and the rate of blocking may change drastically.

2 Simulation method

We use the force coupling method[7] to study the behavior of interacting particles including simultaneously the effect of the carrying fluid flow, direct hydrodynamic interactions and colloidal attraction–repulsion forces between particles and walls. In this method, the presence of particles in the flow is accounted for by localized forcing terms supplemented to fluid flow equations: for Stokes flow (or Navier–Stokes flow for finite Reynolds) standard multipole expansion based on the summation of singularities is extended to model the finite-size of particles (Dirac delta function is left in favor of a localized finite size Gaussian force envelope). This prevents numerical difficulties related to the transport of singularities and provides a good representation of the real size of spherical particles. Only six to eight grid cells are needed to discretize the particle diameter with a good accuracy. The FCM can be implemented in any existing flow solver; it is flexible (see Climent and Maxey[8]) and gives a minor overhead computing time. Once the resolution is fine enough to resolve the Gaussian force envelope, the FCM can accurately reproduce the flow perturbations. When two particles are close to contact, the force coupling method underestimates the lubrication effects. As a result, the FCM has been used mainly for volume fractions lower than 20% while for larger concentrations, lubrication corrections must be implemented[9] (see also the study of Yeo and Maxey[10]).

2.1 Summary of the force coupling method

The basic concept of the FCM relies on the direct resolution of multibody hydrodynamic interactions by solving flow equations including source terms. The force coupling method has been implemented in JADIM (in-house software developed at the IMFT, the Institute of Fluid Mechanics, Toulouse) to solve the fluid flow equations using a finite volume method on a staggered grid (a sketch of the general algorithm using JADIM and the force coupling method is provided in Fig. 1). The fluid is assumed to be incompressible (eqn (1)) with a constant dynamic viscosity μ_f and fluid density ρ_f. Incompressibility of the flow is achieved by a fractional step method using an auxiliary potential and the solution of a Poisson equation. The spatial derivatives are computed with second order accuracy and temporal integration is achieved by a third order Runge–Kutta scheme and a semi-implicit Crank–Nicholson scheme for the viscous terms. At low Reynolds numbers, the left hand side of eqn (2) is negligible and Navier–Stokes equations degenerate to Stokes equations. All particles are modeled by forcing terms (eqn (3)) spatially spread out on Gaussian envelopes (eqn (4)) and added to the momentum equations of the fluid flow.

$$\nabla \cdot u = 0 \tag{1}$$

$$\rho_f \left(\frac{\partial u}{\partial t} + \nabla \cdot uu \right) = -\nabla p + \mu_f \nabla^2 u + f(x,t) \tag{2}$$

In the FCM, the fluid fills the entire volume of the simulation domain. In momentum balance eqn (2), $f(x, t)$ accounts for the perturbation induced by the presence of each particle in the suspension. This force represents also the momentum exchange used in models of two phase flows[11] between the fluid phase and the particles. Each particle n (with the total number N_a) acts on the fluid with the force $F^{(n)}$ (eqn (3)).

$$f_i(x,t) = \sum_{n=1}^{N_a} F_i^{(n)} \Delta\left(x - Y^{(n)}(t)\right) + G_{ij}^{(n)} \frac{\partial}{\partial x_j} \Delta'\left(x - Y^{(n)}(t)\right) \tag{3}$$

where $Y^{(n)}$ is the position of the nth particle center. The first term of the multipole expansion is called the monopole. It is the finite size analog of the pointwise Stokeslet. This force

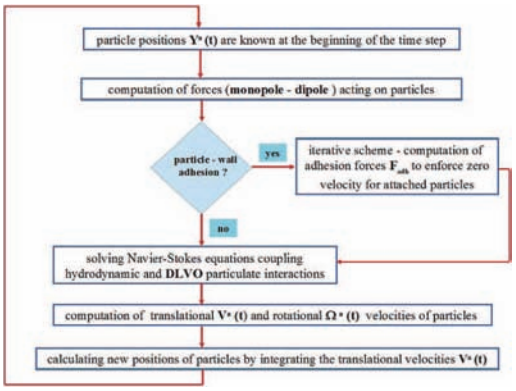

Fig. 1 Sketch of the algorithm including the FCM and inner iterations to solve the resistance problem.

monopole represents the sum of body force, particle–particle and particle–wall interaction forces (adhesive–repulsive–non-overlapping forces). The dipole term, the second term of eqn (3) helps to improve the details of the flow structure close to the particle surface. Its role is to cancel the rate of strain of the local flow within the volume occupied by the particle which behaves as a solid.[12] The Gaussian function Δ or Δ' allows modeling the finite size of the particles with the corresponding length scales σ for $\Delta(x)$ and σ' for $\Delta'(x)$.

$$\Delta\left(x - Y^{(n)}\right) = \left(2\pi\sigma^2\right)^{(-3/2)} \exp\left(\frac{-\left|\left(x - Y^{(n)}\right)\right|^2}{2\sigma^2}\right) \tag{4}$$

Considering the particle radius a, these length scales are set as $a/\sigma = \sqrt{\pi}$ and $a/\sigma' = \left(6\sqrt{\pi}\right)^{1/3}$ respectively. The value of σ is determined analytically to match exactly the Stokes drag on an isolated particle translating in a uniform fluid flow (Maxey and Patel,[7] Climent and Maxey[8]). In the expression of the dipole term, $G_{ij}^{(n)}$ is a tensor which may be decomposed into symmetric and anti-symmetric parts: $G_{ij}^{(n)} = S_{ij}^{(n)} + A_{ij}^{(n)}$. The symmetric part $S_{ij}^{(n)}$, namely the stresslet, contributes to enforce a solid body motion (deformation free) within the fluid occupied by the particle. For several particles, an iterative scheme (conjugate gradient) is used to enforce a zero strain rate (eqn (5)) within the particle volume (see details in the paper by Dance and Maxey[9]).

$$S_{ij}^{(n)} = \frac{1}{2}\int\left(\frac{\partial U_i}{\partial x_j} + \frac{\partial U_j}{\partial x_i}\right)\Delta'\left(x - Y^n(n)\right)\mathrm{d}^3x = 0 \tag{5}$$

The anti-symmetric part $A_{ij}^{(n)}$ (eqn (6)) is related to external torques acting on particles yielding rotation of the fluid as a solid body.

$$A_{ij}^{(n)} = \frac{1}{2}\varepsilon_{ijk}T_k^{(n)} \tag{6}$$

Particles move freely in a Lagrangian framework while their trajectories are solved simultaneously taking into account the local fluid velocity. Translational and rotational velocities of particles are obtained respectively by spatial averaging of the fluid velocity and vorticity. Velocity (eqn (7)) is integrated over the monopole Gaussian envelope Δ while the fluid vorticity (eqn (8)) is integrated over the dipole Gaussian envelope Δ'.

$$V^{(n)}(t) = \iiint u(x, t)\Delta(x - Y^{(n)}(t))\mathrm{d}^3x \tag{7}$$

$$\Omega^{(n)}(t) = \iiint \nabla \times u(x, t)\Delta'(x - Y^{(n)}(t))\mathrm{d}^3x \tag{8}$$

Finally, the particle trajectory is computed by temporal integration of eqn (9).

$$\frac{\mathrm{d}Y^{(n)}(t)}{\mathrm{d}t} = V^{(n)}(t) \tag{9}$$

More details on the theoretical background of the force coupling method and its validation have been reported by Maxey and Patel,[7] Lomholt *et al.*[13] and Lomholt and Maxey.[12]

Concerning the study of suspension flows, the FCM has also been validated for sedimentation problems (Climent and Maxey[14]) and bimodal suspensions (Abbas *et al.*[15]).

2.2 Surface interaction modeling

Non-hydrodynamic particle interactions are taken into account in the simulations by considering DLVO forces. The interaction forces between two rigid bodies are obtained by pairwise summation of molecular forces. For a pair of spherical and homogeneous particles, the expressions of attractive and repulsive forces are given in eqn (10) and (11) (see more details in Feke and Schowalter[16]).

$$F_\mathrm{a} = \frac{4A_\mathrm{h}}{3a}\left(\frac{z}{a} + 2\right)\left(\frac{1}{b_1 b_2} - \frac{1}{2}\left(\frac{1}{{b_1}^2} + \frac{1}{{b_2}^2}\right)\right) \tag{10}$$

$$F_\mathrm{r} = 4\pi\varepsilon_0\varepsilon_\mathrm{r}{\psi_\mathrm{pp}}^2 ka\left(\mathrm{e}^{-kz}\left(\frac{1 - \mathrm{e}^{-kz}}{1 - \mathrm{e}^{-2kz}}\right)\right) \tag{11}$$

where b_1 and b_2 are respectively equal to $(z/a)^2 + 4z/a$ and $(z/a)^2 + 4z/a + 4$. A_h is the Hamaker constant which is related to the physical properties of the particle material and to the ambient fluid, z represents the distance between the particle surfaces, k is the inverse of Debye length, ψ the zeta potential, ε_0 the vacuum permittivity and ε_r is the relative permittivity of the fluid.

Regarding particle–wall interactions, eqn (12) and (13) are obtained from eqn (10) and (11) assuming that one particle radius is infinite. Those expressions are valid provided that the interaction length scale is very small compared to the particle radius. Thereafter, the particle–wall interaction can also be used for particle–wall corner interaction.

$$F_\mathrm{a} = \frac{A_\mathrm{h}}{3a}\left(\frac{1}{b_{11}b_{22}} - \frac{1}{2}\left(\frac{1}{{b_{11}}^2} + \frac{1}{{b_{22}}^2}\right)\right) \tag{12}$$

$$F_\mathrm{r} = 8\pi\varepsilon_0\varepsilon_\mathrm{r}{\psi_\mathrm{pw}}^2 ka\left(\mathrm{e}^{-kz}\left(\frac{1 - \mathrm{e}^{-kz}}{1 - \mathrm{e}^{-2kz}}\right)\right) \tag{13}$$

where b_{11} and b_{22} are respectively equal to z/a and $z/a + 2$. DLVO interparticle forces used for simulations have been scaled by an estimate of the hydrodynamic force ($F_\mathrm{h} = 4U^2\rho_\mathrm{f}\pi a^2$) in the specific flow configuration we investigated (U is the constant velocity at the inlet boundary). This force scale is obtained by considering the drag force acting on a particle in a flow experiencing a sudden restriction of the cross-section (flow through the pore). For particle–particle and particle–wall interactions, the magnitude of van der Waals attraction force A_h/a is constant and equal to $F_\mathrm{h}/125$. The interaction length of the attraction is constant and equal to $0.1a$ throughout all simulations. The electrostatic repulsive force has an interaction distance equal to $4a$ which is fixed by choosing the Debye length. The pre-exponential factor $\varepsilon_0\varepsilon_\mathrm{r}{\psi_\mathrm{pp}}^2$ of eqn (11), noted F_pp (and $\varepsilon_0\varepsilon_\mathrm{r}{\psi_\mathrm{pw}}^2$ of eqn (13) noted F_pw) and representing the appropriate magnitude of particle–particle (and particle–wall) repulsive force is scaled by the hydrodynamic force. To investigate the effect of different physical–chemical properties, the values of those attractive and repulsive forces scales will be varied independently. When

adding repulsive and attractive forces, the maximum of repulsion is located at $0.02a$ while the total interaction force vanishes for distance longer than $4a$. Simulation conditions can represent the behavior of micrometric particles (when Brownian diffusion is negligible) interacting through long-range electrostatic repulsion (interaction distance of the order of the particle size). Such colloidal dispersion can be obtained by dispersing micrometric particles in a solvent having a low dielectric constant and low salt concentration; Debye length and particle size can then stand in the micrometric range.[17]

2.3 Non-overlapping force

When short range particle–particle interactions occur, solid surfaces might come into contact due to the attractive contribution of DLVO forces. In the FCM, the particles are represented by forcing terms in momentum balance equations. Therefore, particle overlapping must be prevented by a steep repulsion force which could represent forces due to the overlapping of electron clouds (Pauli or Born repulsion). We selected the model (eqn (14)) proposed by Drazer *et al.*[18] for short range non-overlapping forces and already well tested in the context of Stokesian dynamics.

$$F_{\alpha\beta} = F_0 \frac{e^{-z/r_c}}{1 - e^{-z/r_c}} e_{\alpha\beta} \tag{14}$$

where F_0 is a force scale, z is the normalized gap between the surfaces of two particles or between the particle and a wall, r_c is the interaction distance and $e_{\alpha\beta}$ is a unit vector along the line of particle centers β to α. The value of F_0 is proportional to the hydrodynamic force ($4U^2\rho_f\pi a^2$). This force has been varied to verify that it has a minor effect on the overall dynamics of the flowing suspension.

2.4 FCM and resistance formulation

The force coupling method is straightforward to solve mobility problems: forces and torques are imposed and particle velocities, rotation rates and trajectories are obtained through the direct solution of Stokes equations. However, when a particle is attached onto a wall, the adhesion force holds this particle fixed. In that case, the condition which has to be satisfied is the zero velocity and the zero rotation rate for the attached particle but the force and torque experienced by the particle are unknown and depend on the local flow and multi-body interactions with other particles. This can be formulated into a resistance problem: the forces acting on all fixed particles depend on hydrodynamic interactions and DLVO forces. They have to meet simultaneously the conditions of zero velocity and zero rotation rate for all attached particles. This is an important feature of our simulations, particles fixed at the wall are allowed neither to slide relative to the wall nor to be re-suspended by the flow (we assume that adhesion is irreversible and a particle touching the wall or an already attached particle remains fixed for the rest of the simulation). To hold particles fixed, an iterative scheme is used to evaluate each adhesion force and torque. This iterative scheme (eqn (15) and (16)) corresponds to solving the resistance problem enforcing the conditions of zero velocity and zero rotation rate for attached particles. At each iteration, Navier–Stokes equations are solved to account for multi-body hydrodynamic interactions.

$$\frac{d^*F_{adh}(t^*)}{dt^*} = -\alpha_1 V(t^*) \tag{15}$$

$$\frac{d^*T_{adh}(t^*)}{dt^*} = -\alpha_2 \Omega(t^*) \tag{16}$$

α_1 and α_2 are numerical penalty parameters which are properly selected to reduce the number of iterations. The iterative scheme is initialized by the solution of a previous time step. When the velocity $V(t^*)$ and the rotation $\Omega(t^*)$ reach the threshold of convergence (typically $10^{-5}U$: where U is equal to unity as the dimensionless fluid velocity at the inlet of the pore) for all fixed particles, the forces (eqn (15)) and torques (eqn (16)) of adhesion are then known and the simulation proceeds to a new physical time step of particles and fluid motion. The overall algorithm including the Force Coupling Method (FCM) is shown in Fig. 1 for one single time step.

2.5 Description of simulation conditions

The simulation domain used to study the behavior of interacting particles at a pore scale is shown in Fig. 2. The dimensions of the simulation domain are $X = 40.32a$; $Y = 24.96a$; $Z = 10.24a$ in the streamwise, crosstream and spanwise directions, respectively. The ratio between the pore size and the diameter of particles is equal to 4 and matches experimental conditions investigated in our previous study.[19] All boundary conditions imposed on the simulation domain are presented in Fig. 2:

- on faces 1–3 (cross-stream direction) and 5–6 (spanwise z direction), periodic boundary conditions are imposed for the fluid flow and particles,

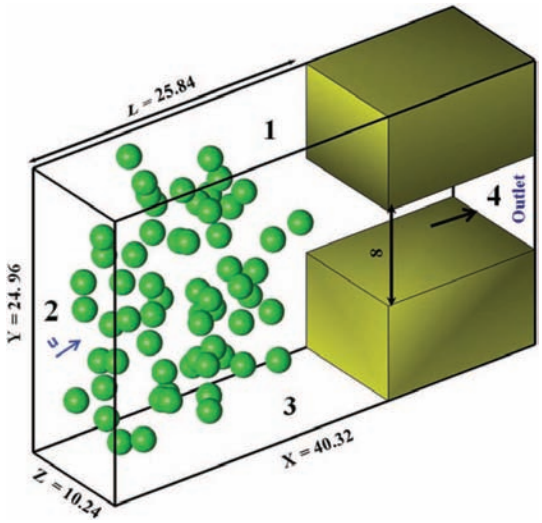

Fig. 2 Schematic view of a 3D pore and the corresponding boundary conditions.

- a constant dimensionless fluid velocity ($U = 1$) is imposed on the inlet section (face 2 where particles are introduced randomly along simulations),

- obstacles (colored in green) on both sides of the pore entrance mimic the cross-section reduction of our experimental microfluidic filtration system,[19]

- face 4 is the outlet section.

All simulations are performed under a constant flow rate and dimensions are scaled using the particle radius a as a characteristic length scale. Fluid flows in a laminar regime for all simulations (pore Reynolds is equal $O(10^{-2})$) and particles are neutrally buoyant. Inertia and gravity effects are negligible. Particles are initially seeded at random non-overlapping positions throughout the pore entrance (face 2). Several draws (typically 3) of the random seeding were carried out and we present average results formed over the three simulations under the same conditions. During simulations, new particles (randomly seeded along $Y - Z$ plane) pass through the inlet face 2 assuming a constant and uniform particulate volume fraction ϕ_0 with constant fluid velocity. This is achieved by seeding particles when a characteristic time $t_{\text{injec}} = (4/3\pi a^3)/(\phi_0 SU)$ is elapsed between two successive injections of particles through face 2 (S is the area). We assume that a strong adhesion force fixes the particles onto the wall or to other attached particles when they come into contact. This contact occurs when the separation distance between two particles is below 10^{-5} a. Once contact occurs, we assume that the particles become adhesive and this adhesion is irreversible. No re-suspension or rearrangement of fixed particles within an aggregate is allowed. While the plug is growing, the solution of the resistance problem yields a progressive increase of the pressure drop between face 2 and 4. The simulation time t_s is made dimensionless using L/U where L is the length from the domain inlet to the pore (see Fig. 2). Ut_s/L can be interpreted as the ratio of the simulation time over the average residence time in the domain just upstream of the pore entrance. It is also a normalized volume of injected fluid (V_{inj}) which passes through the pore along the simulation time. The simulation ends when the pore is completely clogged (any new injection of particles is no longer possible). Particles reaching the outlet boundary leave the simulation freely.

We analyze the effect of the inlet volume fraction of particles (ϕ_0 equals 5–10% to 15–20%) with purely adhesive particles (no DLVO repulsion forces) on the aggregation and clogging phenomena. For a particle concentration equal to 10%, the effect of non-hydrodynamic surface interactions is also studied considering several magnitudes of the repulsive force barrier between particles and particle–wall.

2.6 Simulations post processing

Simulation raw data (particle positions, velocities and forces or flow information) have to be processed for analyzing relevant quantities which may be compared to experiments, theoretical predictions or other numerical models. We have selected a number of macroscopic quantities such as the pore bulk permeability (k in m^2) derived from the Darcy law (17), the hydrodynamic resistance and the capture efficiency of the plug.

The bulk permeability $k(t)$ including the effect of attached particles will be made dimensionless using the reference permeability of the pore completely free of particles (k_0). Based on eqn (17) the adhesion of particles generates the variation of the pressure drop $\Delta P(t)/L$ during clogging.

$$\frac{k(t)}{k_0} = \frac{\mu_f U}{k_0 \Delta P/L} \tag{17}$$

We also propose a description of the microstructure based on the coordination number. The coordination number is an indicator which gives information on the microscopic arrangement of particles in an aggregate. It corresponds to the average number of fixed particles permanently bonded to a reference particle and indicates the type of aggregate structures formed. More details concerning the computation of these macroscopic and microscopic statistics are provided in a previous study[20] on a straight channel blockage.

3 Pore clogging simulations

Direct numerical simulations with the FCM method have been performed for different intensities of surface interactions. The following sections present the results for particle aggregation in simulation obtained for purely adhesive interactions (Section 3.1), for repulsive interactions with a similar magnitude between particles or particles and walls (Section 3.2) and finally, for repulsive interactions with different magnitudes between particle–particle and particle–wall (Section 3.3).

3.1 Clogging under adhesive conditions

In this first set of simulations, we fix the repulsive potential of DLVO forces to zero. Only short range attractive interactions act between particles and between particles and walls: particles can then be considered as sticky.

The evolution of the pore permeability shown in Fig. 3 is scaled using the reference permeability of the pore at $t_s = 0$ (free of attached particles). Time has been plotted in terms of the normalized volume of the injected fluid. For different volume fraction of particles, the permeability reduction is negligible until $V_{\text{inj}} = 0.45$ when the first particle attaches onto the pore initiating blockage (this time corresponds to the duration required for a particle following a critical trajectory to move from the inlet to one of the pore corners[21]). Then, the permeability reduction depends on the inlet value of the particle concentration ϕ_0. For the same value of V_{inj}, the permeability is reduced for larger volume fractions of particles. For a normalized volume of injected fluid equal to 0.8, the normalized permeability is reduced from a high value at $\phi_0 = 5\%$ (0.85 for 11 adhered particles) to a very low value at $\phi_0 = 20\%$ (0.028 for 320 attached particles – see Fig. 4).

The observed variations of permeability in Fig. 3 are the results of the coupling of two mechanisms: the dynamics of the particle capture (Fig. 4 where the number of adhered particles is plotted as a function of the normalized volume of injected fluid) and the hydrodynamic resistance induced by the capture

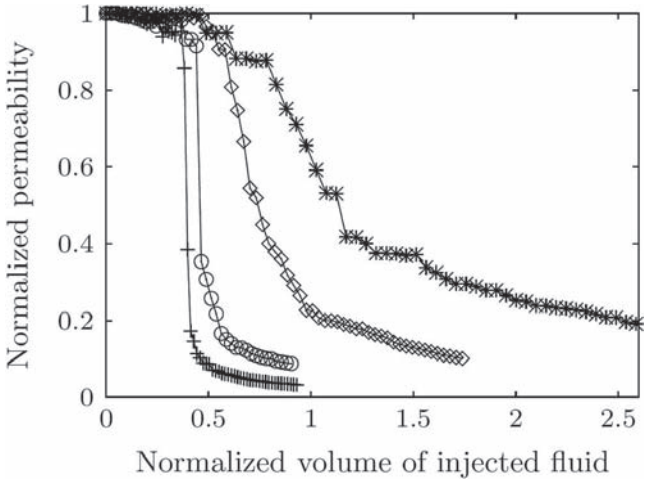

Fig. 3 Evolution of the scaled permeability *vs.* normalized volume of injected fluid for different inlet volume fractions of particles: -*- 5%, -◇- 10%, -○- 15%, and -+- 20%.

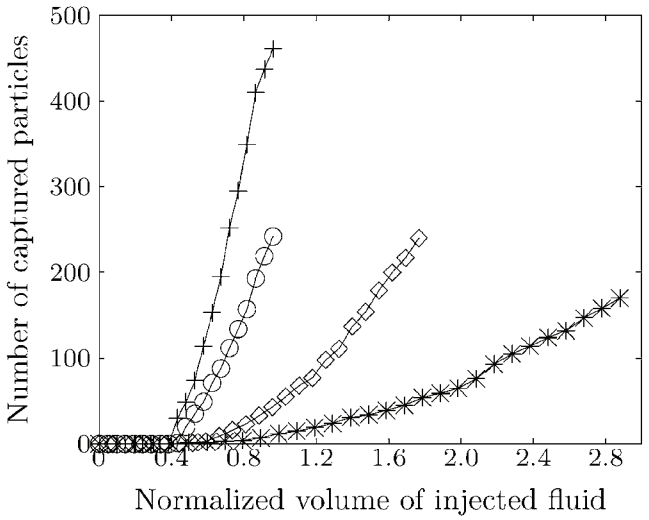

Fig. 4 Evolution of the number of adhered particles *vs.* normalized volume of injected fluid for different inlet volume fractions of particles: -*- 5%, -◇- 10%, -○- 15%, and -+- 20%.

(Fig. 5). Depending on the relative positions of attached particles at the entrance of the pore, the same number of adhered particles yields different hydrodynamic resistances.

For low concentrations, the dynamics of clogging is progressive. For a higher particle concentration, the rapid reduction of the normalized permeability (Fig. 3) can be attributed to a sudden and simultaneous adhesion of a large number of particles at the pore inlet for $\phi_0 = 20\%$ (Fig. 4). This corresponds to a collective effect for these concentrated flowing particles during the aggregation and clogging phenomena.

Fig. 5 presents the evolution of the additional hydrodynamic resistance, $\frac{1}{k(t)} - \frac{1}{k_0}$ (which is inversely proportional to the normalized permeability) as a function of the number of attached particles. For the same number of attached particles equal to 100, the resistance is three times more important when

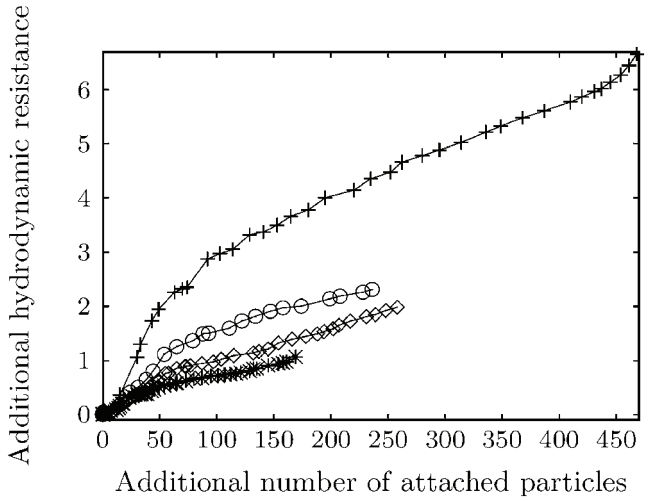

Fig. 5 Evolution of the scaled hydrodynamic resistance *vs.* number of attached particles for different volume fractions of particles: -*- 5%, -◇- 10%, -○- 15%, and -+- 20%.

the clogging is formed at 20% inlet concentration than at 10%. The slope of the curve in Fig. 5 would be constant if the deposit is homogeneous. The change in slope can be attributed to the transition between arch formation (for the first instants of clogging) to the deposit growth (so-called the cake in the filtration process context). This transition will be analyzed in the Discussion (Section 4.1).

Finally, these results show that an increase of concentration has two effects on pore clogging. First, the concentration leads to a more rapid clogging of the pore. Secondly, the structure of the particle aggregate formed at high concentration is less permeable than that formed at a lower concentration. At high concentration, the bridging mechanism[22] induces, in short time, more adhesion of particles in zones of high fluid velocities (entrance of the pore) and yields an important increase of the hydrodynamic resistance (rapid decrease of the bulk permeability).

3.2 Clogging under repulsive particle–particle and particle–wall interactions with similar magnitude

Based on studies showing that surface interactions like DLVO interaction forces can play a significant role in clogging mechanisms,[23] we have carried out simulations on particle aggregation and pore clogging for different magnitudes of surface interaction (the inlet volume fraction of particles is kept fixed and equal to 10%). Particle–particle (F_{pp}) and particle–wall (F_{pw}) interaction forces can be varied independently. However for those present simulations, particle–particle and particle–wall interaction forces are equal and varied by selecting respectively appropriate values for $\varepsilon_0\varepsilon_r{\psi_{pp}}^2$ (eqn (11)) and for $\varepsilon_0\varepsilon_r{\psi_{pw}}^2$ (eqn (13)). In terms of scaled forces, the repulsive forces F_{pp} and F_{pw} have been progressively varied: $10F_h$ – $20F_h$ – $30F_h$ – $60F_h$. The typical values of repulsive forces that we selected allow investigating gradually configurations ranging from pure adhesion (previous section) to strong repulsion corresponding to the absence of particle aggregation or deposit.

Fig. 6 shows the evolution of the normalized permeability in simulation cases where DLVO surface interactions are accounted for. The variation of the bulk permeability is very different from the previous simulation cases under pure adhesion, $F_{pp} = F_{pw} = 0$. For F_{pp} and F_{pw} less than $30F_h$, the decrease in permeability is delayed as the repulsive force increases. When one normalized flow unit has flowed through the pore, the normalized permeability is equal to 0.4 when repulsive interaction is $10F_h$ and this level is reached only after two normalized volumes for a repulsion magnitude $30F_h$. For a force of $60F_h$, the drop in permeability does not occur any longer but fluctuations of the permeability between 0.6 and 1 are observed. These different regimes are related to the dynamics of the particle capture (Fig. 7) and to the hydrodynamic resistance induced by the captured particles (Fig. 8).

Fig. 7 clearly shows that the capture of particle is delayed when the repulsive force increases. Those results can be interpreted in terms of the critical flux concept and will be discussed further in Section 4.3. The results in Fig. 8 indicate that the variation of additional hydrodynamic resistance depends also on the magnitude of DLVO repulsive forces. For the same number of attached particles, the hydrodynamic resistance becomes larger when repulsive forces increase. Such a trend can be investigated by analyzing the 3D spatial structure of captured particles.

Fig. 9 and 10 present a gray scale projection for 100 attached particles: the grey value is relative to the density of particles (as in X-ray imaging). Those visual results would be similar to *in situ* measurement of particle concentration with X-ray tomography. The figure clearly shows different 3D structures of the plug according to the particulate interactions: in the absence of repulsion (Fig. 9), dendritic structures of particles appear whereas in the presence of repulsion (Fig. 10), the deposit is denser and compact. These differences in the clogging structure then induce an important change of hydrodynamic resistance: the structure in Fig. 9 leads to an additional resistance of 1 (see Fig. 8 for 100 adhered particles) whereas the structure in Fig. 10 provokes a resistance of 2.5 for the same number of particles forming the plug.

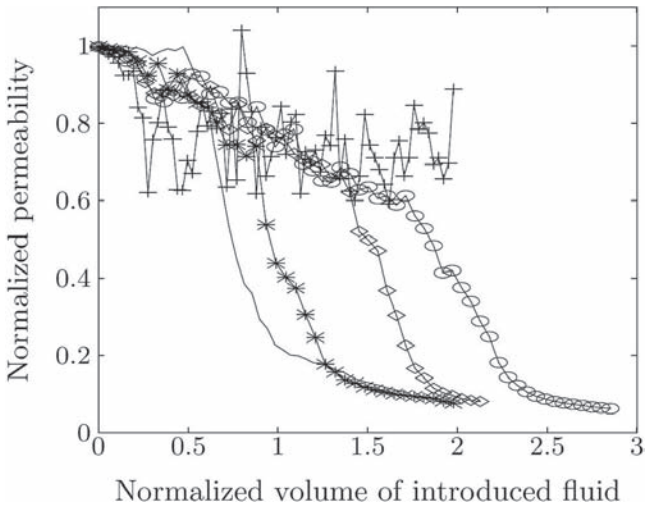

Fig. 6 Evolution of the scaled permeability *vs.* normalized volume of injected fluid for different values of F_{pp} and F_{pw}: – 0, -*- $10F_h$, -◇- $20F_h$, -○- $30F_h$, and -+- $60F_h$.

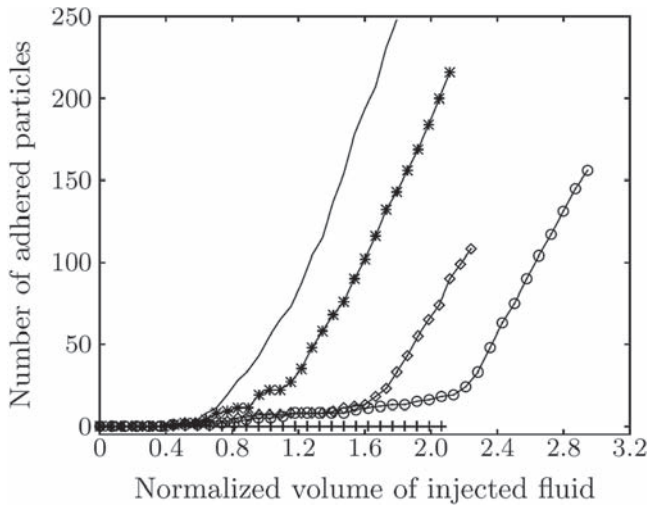

Fig. 7 Evolution of the number of adhered particles *vs.* normalized volume of injected fluid for different values of F_{pp} and F_{pw}: – 0, -*- $10F_h$, -◇- $20F_h$, -○- $30F_h$, and -+- $60F_h$.

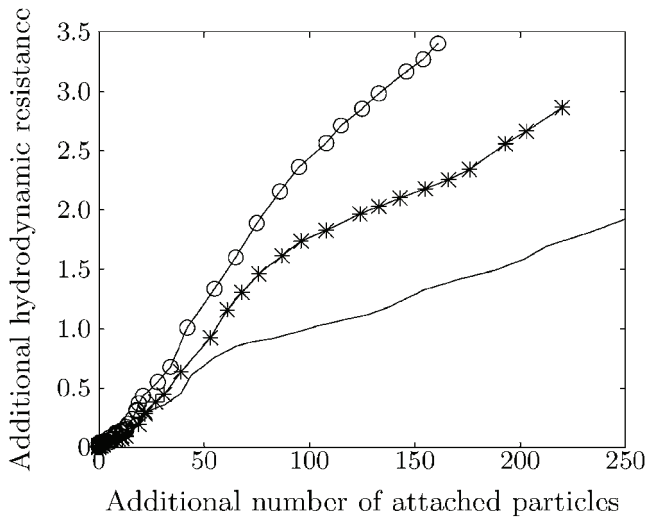

Fig. 8 Evolution of the scaled hydrodynamic resistance *vs.* number of attached particles for different values of F_{pp} and F_{pw}: – 0, -*- $20F_h$, and -○- $30F_h$.

Strong repulsive forces induce successive interactions with attached particles and lead them to adhere in locations where the velocities of the fluid flow are larger (in front of the pore entrance). These results are in good agreement with those obtained by Gassara *et al.*[3] as they studied the effect of hydrodynamic conditions and physical–chemical interactions on the morphology of particle deposits in a Hele Shaw cell (corresponding to a 2D pore), see the Discussion in Section 4.2. A similar effect of colloidal stability on the ordering of concentrated dispersion has also been observed during concentration in microevaporators.[24] The system with repulsive interaction seems to undergo or to approach an ordering transition (a

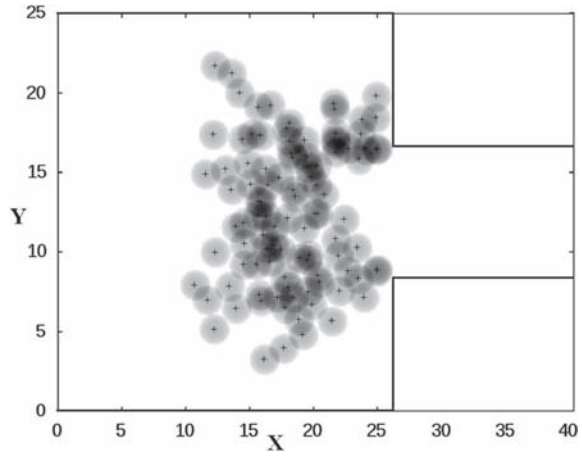

Fig. 9 Side view of the 3D pore with 100 attached particles in the absence of repulsion forces $F_{pp} = F_{pw} = 0$.

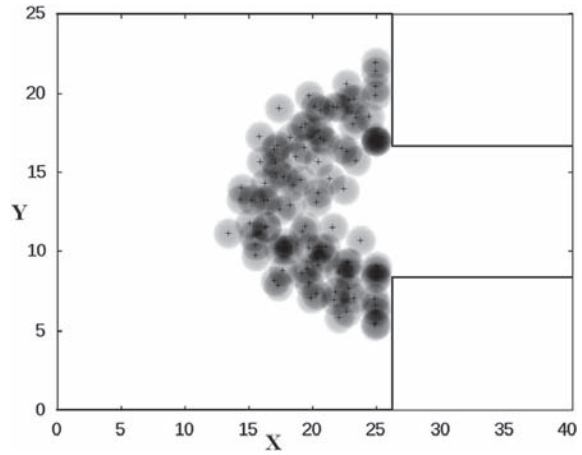

Fig. 10 Side view of the 3D pore with 100 attached particles for $F_{pp} = F_{pw} = 30F_h$.

Wigner glass phase). Such an ordering of repulsive colloids is still possible under non equilibrium conditions as in sheared colloidal dispersion.[25]

3.3 Clogging under particle–particle and particle–wall interactions with different magnitudes

The aggregate structures formed by adhered particles are compared when different values of DLVO repulsive forces between particle–particle and particle–wall ($F_{pp} \neq F_{pw}$) are acting. Fig. 11 summarizes different types of aggregate structures obtained in our simulations for various values of particle–particle (F_{pp}) on the x axis and particle–wall (F_{pw}) interactions on the y axis. The presence of low repulsive forces ($F_{pp} = F_{pw} = 10F_h$) leads to the formation of arches (dendrites) and permeable structures at the end of simulation. Contrarily, for high repulsive forces ($F_{pp} = F_{pw} = 60F_h$), no adhesion of particles is observed: only fluctuations of permeability are observed mainly due to transient accumulation of particles (without adhesion) at the pore entrance. For moderate repulsion strength ($F_{pp} = F_{pw} = 30F_h$),

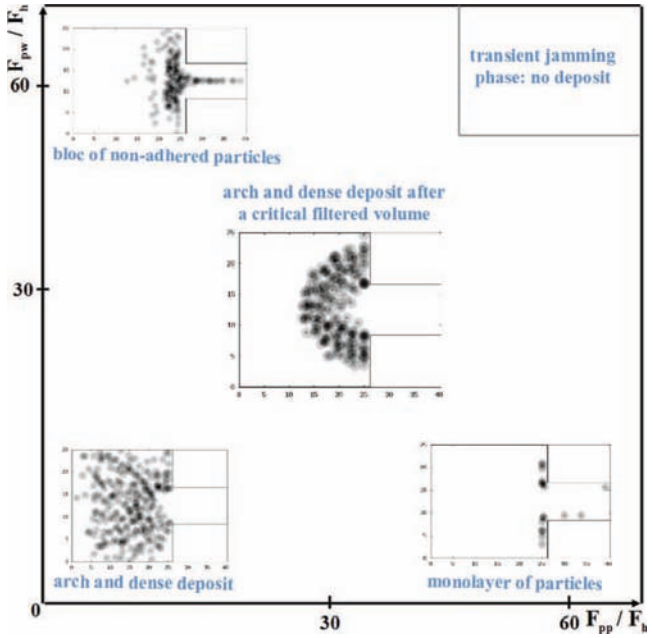

Fig. 11 Aggregate structures of particles for different values of DLVO particle–particle (F_{pp}) and particle–wall (F_{pw}) interaction forces.

the formation of arch and dense deposits occurs only above a critical volume of injected fluid. The critical filtered volume which initiates the adhesion of particles is larger when the repulsive force increases. Under these conditions and when a deposit is formed, the particle structure is compact and its permeability is low. When particle–particle interactions become larger than particle–wall interactions ($F_{pp} \geq 8F_{pw}$), the adhesion of particles onto walls is enhanced. For high repulsion magnitude, only particle monolayers attached onto the walls are observed (similar to monolayer adsorption). After this first layer of deposited particles is formed, new particles are not able to overcome the particle–particle repulsive barrier to form a multilayer deposit. Finally, in Fig. 11, when particle–wall interactions are larger than particle–particle interactions ($F_{pw} \geq 16F_{pp}$), no adhesion of particles onto walls is observed. However, during the filtration process, groups of aggregated particles are formed at the pore inlet: particle aggregation occurs in the bulk forced by the drag acting on particles. This suspended aggregate although not adhered on a particular wall acts as a solid obstacle and induces the decrease of the pore permeability.

4 Discussion

The simulations have shown that particle–particle and particle–wall interactions play an important role in the formation of clogging structures at the pore entrance: collective behaviors of flowing particles are induced by an interplay between multibody DLVO and hydrodynamic forces in a confined geometry. Both the dynamics of the capture and the 3D structures of the plug are modified by this complex coupling. The following sections highlight original features brought out by our simulations.

4.1 Transition between arches and deposit formation

Clogging occurs in several steps: first, the initial deposition of particles more likely close to the corners of the pore, secondly, the formation of an arch across the pore entrance and finally the growth of the deposit in the upstream region. The first step appears in simulations with a specific delay before capture of the first particle which follows a critical trajectory to attachment. During the second step, arches are formed. The particles are captured at the pore entrance in the flow region where the fluid velocity is high. This leads to an important drop in permeability or increase in hydrodynamic resistance. In a third step, the inlet of the 3D pore is completely blocked by the arches and any new particles will be collected by the plug forming the deposit. Then, the deposit grows upstream as the simulation time goes on.

Such a scenario is illustrated by a slope change of the evolution of hydrodynamic resistance as a function of the number of adhered particles (in Fig. 12, it happens when the number of adhered particles is around 75). The capture of particles (less than 75) forming the arches leads to pressure drop because the fixed particles are located in a region where the flow velocity is high (the force exerted by the particle on the fluid is then strong). Later on, slope change also occurs in the variation of the hydrodynamic resistance. The additional particles are captured in regions where the flow is homogeneous and the velocity lower than at the pore entrance: the slope in Fig. 12 is then lower and represents the specific resistance of the cake deposit. Similar behavior has been observed at a smaller scale for filtration of the protein through a 0.2 micrometer membrane: Ho and Zydney[26] interpreted these results with a model that accounts for initial fouling due to pore blockage and subsequent fouling due to the growth of a protein cake over initially blocked regions. The transition from the cluster to the cake structure is also demonstrated by Tsutomu *et al.*[27] when they studied the effect of the pore size in membrane fouling using a two-way coupling model taking into account particle–fluid interactions. This method modeled a membrane with regularly spaced straight pores, which are assumed to be track-etched pores. For the same pore–particle size ratio of 2.5 as our simulations, they show a fouling regime in which particles are accumulated on the surface of the membrane without filling the pores. A cake layer forms across the entire filtration area. On the other hand, their results show that a larger pore size membrane (equal to $3.6d_p$: d_p diameter of particle) leads to a fouling mode in which particles filled initially the pores and then formed a cake layer on the surface of the membrane.

Fig. 12 associates also the aggregate structures of particles observed in simulations with the evolution of the additional hydrodynamic resistance. The formation of arches is obtained for a number of adhered particles equal to 75. Such a cluster structure is similar to the one visualized by Agbangla *et al.*[19] at the entrance of a microchannel in microfluidic devices (Fig. 13) for a similar pore/particle size ratio. The dynamics of arch formation changes when the inlet volumetric fraction of particles varies. For a high particle concentration ($\phi_0 = 20\%$), the arch formation occurs sooner and more suddenly as observed in simulations. Such a trend highlights a collective effect of particles inducing the bridging phenomenon at the pore entrance to form arches as described by Ramachandran and Fogler.[22] The bridging phenomenon induces a sudden and instantaneous reduction of the normalized permeability at a high volume fraction of particles.

After the slope change of the hydrodynamic resistance, when the simulation domain is completely blocked, a cake structure of particles occurs. These cake aggregates are similar to the structures observed experimentally by Kosvintsev *et al.*[28] when they studied the behavior of latex particles (diameter equal to 0.4 μm) in dead-end filtration (varying particle concentration and pressure drop) through a membrane pore.

4.2 3D structure of clogging: influence of operating conditions

The 3D structure of the plug is drastically dependent on the operating conditions. Simulations show significant the effect of the particle concentration and of the surface interactions. The permeability of the resulting structure is clearly reduced when the concentration of the dispersed particles flowing through the pore is increased under pure adhesion (Fig. 3). The 3D structure is more compact under high repulsion (Fig. 10).

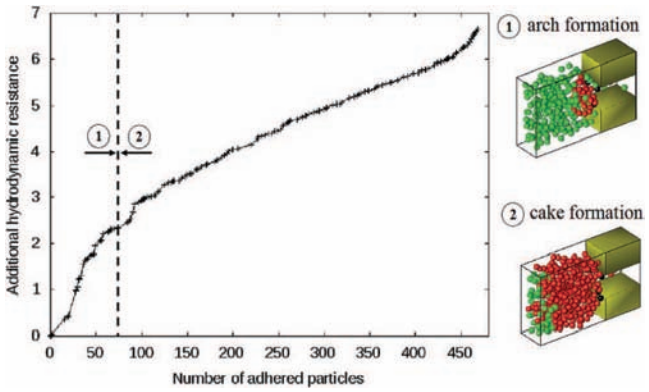

Fig. 12 Evolution of the additional resistance as a function of the number of adhered particles: transition between arches and the cake formation.

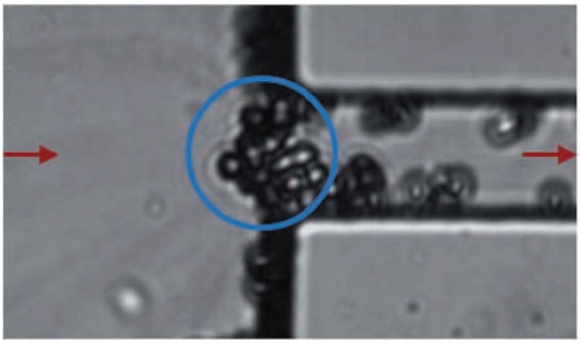

Fig. 13 Observation of the arch formation at the entrance of a microchannel device.[19]

Without repulsive interaction or under low repulsive forces ($F_{pp} = F_{pw} = 10F_h$), particles follow the fluid streamlines with velocity prescribed by the confined flow geometry. Dendritic and permeable structures (Fig. 9) are then formed at the pore inlet. They are similar to loose aggregates observed by Payatakes *et al.*[29] in their study of aerocolloidal particle motion through fiber filters. These heterogeneous microstructures act as collectors and progressively lead to the complete blockage of the pore. A dendritic structure obtained in simulation is characterized by a strong occurrence of the coordination number equal to 2.

The presence of strong repulsive forces ($F_{pp} = F_{pw} = 30F_h$) induces a different arrangement of captured particles. Flowing and interacting particles move across streamlines due to the successive repulsions between particle–particle and particle–wall. Once in contact (irreversible adhesion), they form a compact and dense aggregate (cluster structure) located at the pore inlet as shown in Fig. 10. For compact structures, a high occurrence of coordination numbers equal to 1 appears for particles on the outer region of the dense aggregate, and 3 within the cluster core.

These 3D structures are in agreement with the microstructures of aggregates simulated with Stokesian dynamics and Brownian dynamics under different hydrodynamic conditions and inter-particle potentials.[30] Such formation of dendritic or dense and compact structures of deposit has already been described by the dynamic capture model.[31] The model describes the dynamics of the capture of interacting particles at a membrane surface by defining exactly a capture (collision) zone of injected particles. This model has been validated experimentally by Houi and Lenormand[32] with the study of dilute mud flow through membrane filtration. Taking into account the magnitude of the capture angles, the role of the interplay between physical–chemical and hydrodynamic forces is highlighted in this study. Our simulations confirm this observation related to the interplay between the surface interactions and hydrodynamics without using a critical capture angle.

4.3 Critical conditions of deposition with repulsive forces

In the presence of strong repulsive forces, the clogging dynamics does not only depend on the flow driving force but critical conditions also have to be met for deposition: the driving force has to overcome repulsive barriers to induce the adhesion of particles (first the particle–wall barrier and then the particle–particle barrier). Simulations show the existence of a critical filtered volume above which the clogging starts to be noticeable (Fig. 7): collective behavior between interacting particles induces the formation of a compact and dense structure following the primary injection of particles. Such a critical filtered volume has been already observed experimentally when filtering stable dispersion of latex or clays particles (with strong inter-particles repulsion) with a constant imposed flux on an ultrafiltration membrane under dead-end conditions (Bessiere *et al.*[33]).

To explain such a collective mechanism, it is necessary to understand the effect of the repulsive particle–wall interaction on an isolated particle approaching the pore. In Fig. 14, particle trajectories are plotted for repulsion force F_{pw} equal to $30F_h$ when the normalized fluid velocity imposed at the inlet of the pore is equal to 1. Then, we varied the inlet flow velocity to test the effect of particle blockage at the entrance of the pore. The response of the particle is compared to the analysis of Kim *et al.*[34] In the absence of repulsive forces, we note that the particle moves through the pore following the flow streamline (dotted lines in Fig. 14 for two distinct initial positions). When repulsion is enabled, the particle trajectory is completely different. For any initial position of the particle, the trajectory starts by following the flow streamline and finally migrates when the particle approaches the pore walls. This corresponds to the typical distance of repulsion barrier fixed by the Debye length.

When the fluid velocity is imposed $U = 1$ at the inlet of the simulation domain, the hydrodynamic force acting on a single particle is not strong enough to overcome the repulsion barrier originating from the corners. The particle reaches an equilibrium position on the symmetry axis of the simulation domain ($Y = 12.5$) just upstream of the pore (dashed line in Fig. 14) where repulsion and hydrodynamic forces are balanced. Upon increasing the fluid velocity to $U = 1.5$ the hydrodynamic force overcomes repulsion and the particle (for any initial position) passes through the pore (solid line in 14) towards the channel exit. Such simulation demonstrates the existence of a critical flow velocity for the passage of the particle through the pore as already discussed by Bacchin *et al.*[4] and Kim *et al.*[2] For particle–wall repulsive forces $F_{pw} = 30F_h$, we can expect a critical normalized velocity of the fluid flow (between 1 and 1.5) above which the particle can pass through the pore. This critical fluid

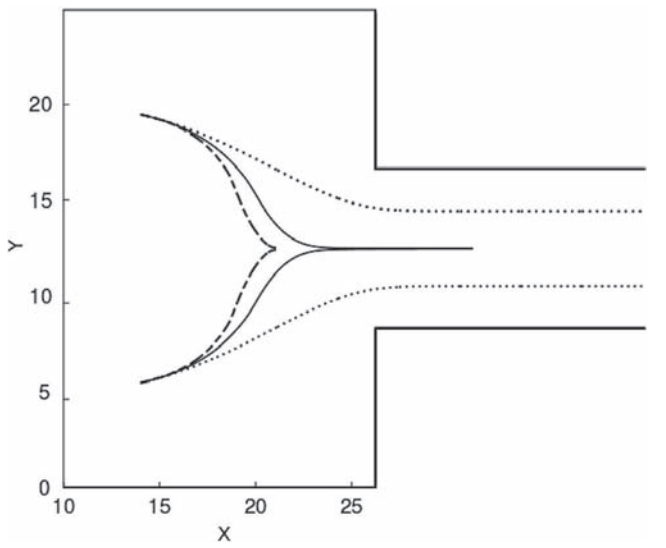

Fig. 14 Different particle trajectories with fixed values of DLVO repulsive force, $F_{pw} = 30F_h$. Trajectories are shown for different values of the normalized velocity and different initial positions. $U = 1$: the particle reaches an equilibrium position in front of the pore (dashed line), $U = 1.5$: the particle passes through the pore (solid line). The dotted line stands for the flow streamline and corresponds to the particle trajectory without repulsion force.

velocity increases while considering stronger particle–wall interaction forces.

Similar simulations performed with several particles show that the accumulation of other particles in the neighborhood of the particle initially blocked at the equilibrium position (for $U = 1$ in Fig. 12) can induce the passage of the first particle. The additional drag force exerted by the flow on both particles helps the first particle to pass through repulsion barriers by an 'interaction–pushing effect'. This is the reason why a given number of particles need to accumulate prior to the pore clogging. Such an 'interaction–pushing effect' has already been described by other studies in 1D (Harmant and Aimar[35]) or in 2D (Kim and Zydney[2]). This trend is illustrated in Fig. 15 where the conditions for clogging are plotted as a function of the normalized volume of the injected fluid. Below the curve of this diagram, filtration conditions (high repulsion and low injected volume or filtration time) do not lead to attachment. The critical conditions are then dependent on the surface interactions and filtered volume: for a given repulsive interactions, the clogging appears when a critical volume of fluid is injected. The simulations results are in a good agreement with the critical operating conditions for deposition that have been observed experimentally in dead-end filtration of stable dispersions with the membrane (Bessiere *et al.*[33]) or within microchannels (Agbangla *et al.*[19]).

4.4 Transient jammed network of repulsive particles at the pore entrance

For high repulsive interactions ($F_{pp} = F_{pw} = 60F_h$), no particle adhesion at walls occurs but we observed fluctuations of the permeability. Although many particles have been injected, the hydrodynamic force is not able to overcome the repulsive barriers towards irreversible adhesion. Based on dynamic visualizations of the particle motion (see ESI†), we have noted that the particle motion experiences successive periods of accelerations and velocity reductions. It means that the dispersion approaches the jamming transition. The permeability fluctuations result then from the transient formation of cluster stabilized by repulsive forces in front of the pore: particles form a network due to repulsive forces (like in repulsive colloidal gels or in Wigner glass) and resist the flow. Under hydrodynamic forcing this network resists (the permeability decreases) and suddenly, the network collapses yielding permeability increase. This effect has been confirmed by analyzing the statistics of the FCM monopole (essentially the force exerted by the particles onto the fluid). These monopole forces reach large values (when the permeability is lower during the fluctuations) and highlight the resistance of particles onto the flow. These fluctuations are the signatures of the dynamical inhomogeneities or caging transport behavior that occurs before colloidal glass transition.[36] This transient repulsive 'gelled' network (or jamming phase) could be the precursor for the formation of the deposit which can form ordered colloidal crystals when the magnitude of particle–particle repulsions is important.

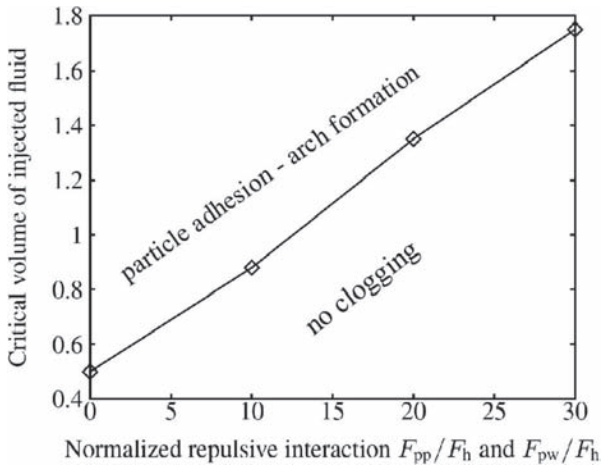

Fig. 15 Diagram of critical conditions leading to pore plugging with repulsive particles.

4.5 Scenario for pore clogging by interacting particles

Our results contribute to a better understanding of the formation of deposit at the pore entrance. A scenario with different steps is proposed in Fig. 16. During initial times of filtration (step 1 in Fig. 16), particles move freely through the pore (no significant interactions between particles because of the dilute regime of the suspension flow). When accumulation increases, we can observe the build-up of a particulate network similar to a Wigner glass phase in which particles interact through pairwise long-range repulsion forces: the electrostatic repulsion keeps the particles apart and produces a transition to an arrested state at the pore entrance. The particle velocities are reduced and slip when the fluid flow appears (step 2). The permeability slightly decreases because of the feedback drag force exerted by the particles on the fluid. A network with a force chains due to interparticle interactions is created: each particle within the force chain has roughly balanced forces on either side. The occurrence of a network is classical for jamming systems[37] which are compatible with the Wigner glass transition.[38] When the network width increases, the cumulative force acting on particles just in front of the pore entrance is stronger: the force chain network is not strong enough to support the cumulative stress. The particles near the pore entrance experience a strong force through repulsive interactions with all upstream particles *via* the 'interaction–pushing effect' (step 3). For a critical number of particle layers, this force can be strong enough to push the particle through the pore overcoming the wall repulsive barrier. The glass phase then collapses and leads to local particle accelerations. Then, two distinct scenarios can be considered according to the magnitude of particle–wall interactions. If the particle–wall interactions are overcome, the particles will adhere onto the walls (step 4). This event can be the precursor for the adhesion of new particles to form arches and then the dense deposit (step 5). It can be also possible to form arches in one single step during the glass collapse: particles at different locations in the network layers can be captured simultaneously to form arches. This mechanism of particle

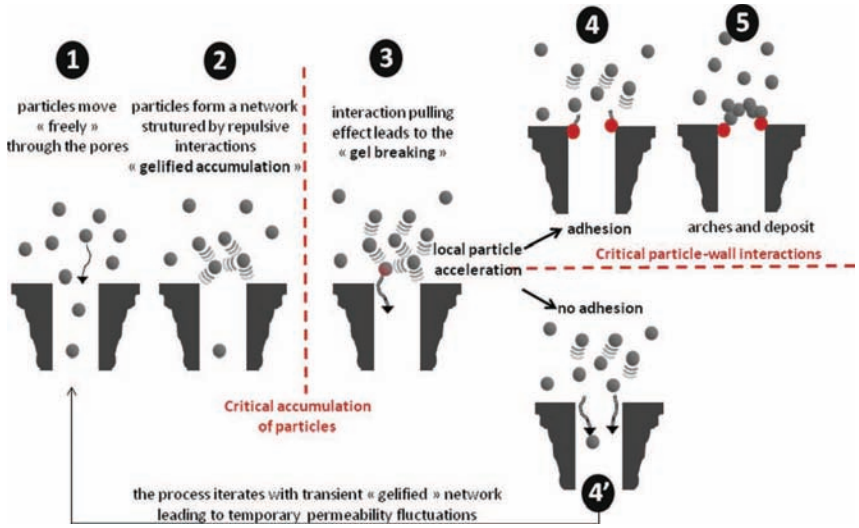

Fig. 16 Scenario for the mechanism of pore plugging with repulsive particles.

bridging, investigated by Ramachandran and Fogler[22] can lead to arches and dense deposit formation as discussed in Section 4.1.

In the presence of large particle–wall interaction forces, repulsion can prevent the particle adhesion following the glass collapse (step 4′). In this case, the glass phase organization is modified (the permeability increases) and a new accumulation can start. This scenario has been simulated in the case of large particle–wall interactions which leads to permeability fluctuations as discussed in Section 4.4. Furthermore, those two scenarios highlight the important role played by the volume of injected fluid and the non-hydrodynamic forces on the aggregation of particles and consequently clogging.

5 Conclusion

Using the force coupling method to account for hydrodynamic and colloidal surface interactions (DLVO forces), the dynamics of the 3D pore clogging and collective effects of interacting particles are simulated and discussed. The set of simulations were obtained for a constant fluid flow rate. With pure attractive forces, we showed the transition from cluster-dendrites (initially formed from the walls or corners) at the pore inlet to cake structures (complete blockage of the pore) at the end of simulations. The inlet particle concentration has a major effect on the dynamics of the adhesion of particles and on the variation of the bulk permeability. For a low inlet volumetric fraction of particles ($\phi_0 = 5\%$) successive depositions of particles on walls or on other adhered particles are observed. The occurrence of the bridging phenomenon (simultaneous adhesion of several particles) induced by the collective effect of flowing particles for $\phi_0 = 20\%$ leads to the rapid and sudden reduction of the normalized permeability.

For simulations performed in the presence of DLVO repulsive forces, a critical volume of injected fluid is required to initiate the adhesion of particles at the pore inlet. This critical volume is larger when the magnitude of repulsive interactions increases. With very strong repulsion ($F_{pp} = F_{pw} = 60F_h$), no adhesion of particles occurs in simulations. However, temporal fluctuations of the bulk permeability periodically occur. These fluctuations are the result of the rearrangement of flowing particles interconnected by DLVO forces. With distinct values of particle–particle (F_{pp}) and particle–wall (F_{pw}) interactions various types of structures are observed such as particle monolayers adhered only to walls for $F_{pp} \geq 8F_{pw}$ and a group of particles suspended at the pore inlet for $F_{pw} \geq 16F_{pp}$. Both the spatial structures of the plug and the capture kinetics are tightly related to the interplay between colloidal surface interactions and hydrodynamics; a scenario for pore clogging mechanism is then proposed.

Nomenclature

a	Particle radius, m
ρ_f	Density of the fluid, kg m^{-3}
μ_f	Dynamic viscosity of the fluid, Pa s
p	Pressure in the fluid, Pa
u	Fluid velocity, ms^{-1}
x	Position in the fluid, m
Δ and Δ'	Gaussian envelope of momentum source terms, m^{-3}
σ and σ'	Width of the Gaussian envelopes, m
$S_{ij}^{(n)}$	Symmetric part of the dipole strength tensor, N m^{-1}
$A_{ij}^{(n)}$	Anti-symmetric part of the dipole strength tensor, N m^{-1}
d_x^3	Elementary volume, m^3
$F^{(n)}$	Force monopole strength due to the nth particle, N
$Y^{(n)}$	Center position of the nth particle, m
$V^{(n)}$	Velocity of the nth particle, m s^{-1}
$\Omega^{(n)}$	Rotation rate of the nth particle, rad s^{-1}
F_a	Attractive force between two particles, N
F_r	Repulsive force between two particles, N
A_h	Hamaker constant, J
$\varepsilon_0\varepsilon_r$	Fluid permittivity, C^2 J^{-1} m^{-1}

ψ	Electrical potential surface, V
k	Inverse of the Debye length, m^{-1}
z	Distance between the center of two particles, m
$F_{\alpha\beta}$	Steep repulsion force, N
F_{adh}	Adhesion force holding fixed particles, N
T_{adh}	Adhesion torque, N m
t_s	Characteristic time of simulation, s
F_h	Hydrodynamic force, N
F_{pp}	Repulsive force between particles, N
F_{pw}	Repulsive force between particles and walls, N
ϕ	Volume fraction of particles

References

1 B. Mustin and B. Stoeber, *Microfluid. Nanofluid.*, 2010, **9**, 905–913.
2 M. M. Kim and A. L. Zydney, *Chem. Eng. Sci.*, 2005, **60**, 4073–4082.
3 D. Gassara, P. Schmitz, A. Ayadi and M. Prat, *Sep. Sci. Technol.*, 2008, **43**, 1754–1770.
4 P. Bacchin, P. Aimar and V. Sanchez, *AIChE J.*, 1995, **41**, 368–376.
5 C. Henry, J. Minier and G. Lefèvre, *Adv. Colloid Interface Sci.*, 2012, **185–186**, 34–76.
6 P. Bacchin, A. Marty, P. Duru, M. Meireles and P. Aimar, *Adv. Colloid Interface Sci.*, 2011, **164**, 2–11.
7 M. Maxey and B. Patel, *Int. J. Multiphase Flow*, 2001, **27**, 1603–1626.
8 E. Climent and M. Maxey, *The Force Coupling Method: A flexible approach for the simulation of particulate flows, inserted in 'Methods for creeping flows'*, ed. F. Feuillebois and A. Sellier, Ressign Press, 2010.
9 S. L. Dance and M. R. Maxey, *J. Comput. Phys.*, 2003, **189**, 212–238.
10 K. Yeo and M. R. Maxey, *J. Comput. Phys.*, 2010, **229**, 2401–2421.
11 H. M. Vollebregt, R. G. M. V. D. Sman and R. M. Boom, *Soft Matter*, 2010, **6**, 6052–6064.
12 S. Lomholt and M. R. Maxey, *J. Comput. Phys.*, 2003, **184**, 381–405.
13 S. Lomholt, B. Stenum and M. R. Maxey, *Int. J. Multiphase Flow*, 2002, **28**, 225–246.
14 E. Climent and M. R. Maxey, *Int. J. Multiphase Flow*, 2003, **29**, 579–601.
15 M. Abbas, E. Climent, O. Simonin and M. Maxey, *Phys. Fluids*, 2006, **18**, 121504.
16 D. L. Feke and W. R. Schowalter, *J. Fluid Mech.*, 1983, **133**, 17–35.
17 D. El-Masri, T. Vissers, S. Badaire, J. Stiefelhagen, H. R. Vutukuri, P. Helfferich, T. H. Zhang, W. Kegel, A. Imhofa and A. van Blaaderen, *Soft Matter*, 2012, **8**, 6979.
18 G. Drazer, J. Koplik, B. Khusid and A. Acrivos, *J. Fluid Mech.*, 2004, **511**, 237–263.
19 G. Agbangla, E. Climent and P. Bacchin, *Sep. Purif. Technol.*, 2012, **101**, 42–48.
20 G. Agbangla, P. Bacchin and E. Climent, *Comput. Fluids*, 2014, **94**, 69–83.
21 H. M. Wyss, D. L. Blair, J. F. Morris, H. A. Stone and D. A. Weitz, *Phys. Rev. E: Stat., Nonlinear, Soft Matter Phys.*, 2006, **74**, 061402.
22 V. Ramachandran and H. S. Fogler, *J. Fluid Mech.*, 1999, **385**, 129–156.
23 H. N. Unni and C. Yang, *Adv. Colloid Interface Sci.*, 2005, **291**, 28–36.
24 A. Merlin, J. B. Salmon and J. Leng, *Soft Matter*, 2012, **8**, 3526–3537.
25 E. Nazockdast and J. F. Morris, *Soft Matter*, 2012, **8**, 4223–4234.
26 C. Ho and A. L. Zydney, *J. Colloid Interface Sci.*, 2000, **232**, 389–399.
27 A. Tsutomu, A. Kazuki, N. Shin-ichi and F. Masahiro, *J. Membr. Sci.*, 2012, **392–393**, 48–57.
28 S. Kosvintsev, R. G. Holdich, I. W. Cumming and V. M. Starov, *J. Membr. Sci.*, 2002, **208**, 181–192.
29 A. Payatakes and L. Gradon, *AIChE J.*, 1980, **26**, 443–454.
30 X. J. Cao, H. Z. Cummins and J. F. Morris, *J. Colloid Interface Sci.*, 2012, **368**, 86–96.
31 P. Schmitz, B. Wandelt, D. Houi and M. Hildenbrand, *J. Membr. Sci.*, 1993, **84**, 171–183.
32 D. Houi and R. Lenormand, *Filtr. Sep.*, 1986, **23**, 238–241.
33 Y. Bessiere, N. Abidine and P. Bacchin, *J. Membr. Sci.*, 2005, **264**, 37–47.
34 M. M. Kim and A. L. Zydney, *J. Colloid Interface Sci.*, 2004, **269**, 425–431.
35 P. Harmant and P. Aimar, *Colloids Surf., A*, 1998, **138**, 217–230.
36 W. K. Kegel and A. V. Blaaderen, *Science*, 2000, **287**, 290–293.
37 C. S. O'Hern, S. A. Langer, A. J. Liu and S. R. Nagel, *Phys. Rev. Lett.*, 2001, **86**, 111–114.
38 P. Levitz, E. Lecolier, A. Mourchid, A. Delville and S. Lyonnard, *Europhys. Lett.*, 2000, **49**, 672.